RSC Advances

PAPER

View Article Online
View Journal | View Issue

Cite this: *RSC Adv.*, 2025, **15**, 41967

A poly(3-methylthiophene)/borophene hybrid for tartaric acid detection

Shahzad Ahmed, [abc] Sonal Gupta,[bc] Arshiya Ansari, [a] Tanmay Suresh More,[d] Andrey N. Kuzmin, [c] Amitava Banerjee, *[a] Devendra Singh Negi, *[a] Pranay Ranjan, *[a] Mark T. Swihart *[cd] and Paras N. Prasad *[bc]

Received 21st June 2025
Accepted 20th October 2025

DOI: 10.1039/d5ra04426j

rsc.li/rsc-advances

Tartaric acid (TA), a key organic acid in grapes and wine, is closely linked to taste quality and human health, making its accurate detection highly important. In this work, we report a borophene/poly(3-methylthiophene) (P3MTP) hybrid electrode fabricated *via* solvent-mediated exfoliation of borophene and electropolymerization of P3MTP on indium tin oxide (ITO) glass. The modified electrode was evaluated by cyclic voltammetry and interference studies, showing a wide linear detection range (5–300 μM), a low detection limit (LOD) (4 μM), and high selectivity toward TA. The sensor also demonstrated excellent stability. In addition, the sensor demonstrated reproducibility with a relative standard deviation (RSD%) of 1.70%. Furthermore, molecular simulations clarified the interaction mechanism between TA, borophene, and P3MTP, explaining the observed electrochemical interaction. These findings highlight the potential of borophene-polymer hybrids as efficient sensing platforms for food quality control and health monitoring.

1 Introduction

TA is a naturally occurring organic acid abundant in grapes,[1–4] where it largely contributes to wine tartness.[5] It is also found in bananas, tamarinds, and other fruits, imparting a characteristic sour taste. TA has been employed with citric acid in effervescent salts to improve the flavor of oral medications.[6,7] Its identification in fruit products is important for assessing ripeness, authenticity, and microbial changes during storage.[8,9] Additionally, TA is widely used in food and beverages, including soft drinks, juices, confections, and baking powder,[10,11] making its detection vital for quality control and labeling.[12] Beyond food applications, TA plays a role in research studies[13] and is a key metabolite in humans, where abnormal levels are linked to adverse health effects.[14–16]

Several approaches have been proposed for evaluating TA, both qualitatively and quantitatively. These approaches include techniques such as gas chromatography (GC),[17] high-performance liquid chromatography (HPLC),[18] near-infrared (IR),[19] visible,[20] and terahertz[21] spectroscopies. However, these methods typically demand costly instrumentation, labor-intensive sample preparation, and highly trained personnel, thereby limiting their accessibility for routine or field-based testing. Furthermore, many traditional techniques, including gravimetric analysis, potentiometry, and capillary electrophoresis, often exhibit issues such as low reproducibility, prolonged analysis durations, and insufficient sensitivity, particularly when differentiating between isomeric forms of TA or analyzing complex sample matrices.[22] For example, several conventional methods used to determine tartaric acid in wine residues are often characterized by lengthy procedures, laborious workflows, and limited reproducibility, underscoring the need for more robust and efficient analytical approaches.[22] Nevertheless, electrochemical biosensors present notable benefits compared to alternative methodologies, including sensitivity, rapid response time, and capacity for selective identification of specific analytes.[23,24] Miniaturization enables the implementation of many of these devices, detecting different substances, into a portable unit. This is important for point-of-care and portable contexts, whereas their affordability and user-friendliness render them applicable in diverse environments.[25] Moreover, electrochemical biosensors facilitate continuous monitoring of analytes in real-time, which is essential for monitoring and control of dynamic processes.[26] Overall, electrochemical biosensors are adaptable and effective tools for addressing analytical and diagnostic requirements in many fields, such as healthcare and environmental monitoring.[27,28] For example, in one study, Ahmed *et al.*[29] developed an electrochemical sensor for histamine detection using an

[a]*Department of Materials Engineering, Indian Institute of Technology Jodhpur, Jodhpur, Rajasthan-342030, India. E-mail: amitava@iitj.ac.in; devendra@iitj.ac.in; pranay.ranjan@iitj.ac.in*

[b]*Department of Chemistry, University at Buffalo, SUNY, New York 14260, USA. E-mail: pnprasad@buffalo.edu*

[c]*The Institute for Lasers, Photonics, and Biophotonics/Chemistry, The State University of New York at Buffalo, Buffalo, New York 14260, USA. E-mail: swihart@buffalo.edu*

[d]*Department of Chemical and Biological Engineering, University at Buffalo, The State University of New York, Buffalo, NY 14260, USA*

inverse opal scaffold and molecularly imprinted polymer (MIP), achieving a linear detection range of 50 nM to 500 μM and a detection limit of 1.07 nM. In another study, Ahmed *et al.*[30] created an electronic tongue for rapid capsaicin detection, which is responsible for the spiciness of chili peppers. This sensor demonstrated linear detection ranges from 0.01 μM to 50 μM and 50 μM to 500 μM, with a detection limit of 2.1 nM. In a separate study, Khan *et al.*[31] developed a self-healing hydrogel-based artificial BioE-Tongue which features mucin as a secreted protein, sodium chloride as an ion-transporting electrolyte, and chitosan/poly(acrylamide-*co*-acrylic acid) as the primary 3D hydrogel network. It was intended to replicate the human tongue's ability to detect astringent and bitter sensations through cyclic voltammetry (CV) measurements. Furthermore, Pei *et al.*[32] demonstrated the electrochemical detection of TA by covalently attaching L/D-cysteine to nitrogen-doped graphene quantum dots, which were then drop-casted onto a glassy carbon electrode (GCE), highlighting a promising approach for TA detection.

Nanostructured materials and polymers are widely studied for their unique properties and applications in medicine, electronics, energy, and environmental science.[33–37] Electrochemical synthesis, also known as chemical polymerization, is commonly used to create conducting polymers, offering precise control over film thickness, shape, and composition.[38–42] Conducting polymers like P3MTP, synthesized from the monomer 3-methylthiophene, are notable for their conductivity, chemical stability, and biocompatibility, making them ideal for biosensing applications.[43–47] P3MTP can be used in devices that detect various biological analytes, including proteins, enzymes, nucleic acids, and small molecules.[46,47]

Borophene, a 2D Xene material alongside phosphorene and silicene,[48] exhibits strong anisotropy due to its 2-dimensional nature.[48,49] Its edge configuration governs transport properties, and its Young's modulus exceeds that of graphene.[50] Structurally, borophene occurs in hexagonal (X_3) or ridged β_{12} phases,[51] with the latter promoting electron transport and analyte anchoring for enhanced bio-analyte detection.[52] Owing to its high surface area, unique electronic features, and proven integration in electrochemical biosensors, borophene-based hybrids are promising for chemical and biological sensing, as summarized in Table S1.

We present here the development of an electrochemical sensor that relies on a borophene/P3MTP hybrid system with the objective of detecting TA levels essential for ensuring food quality and accurate food categorization. Our research aimed to develop a precise method for measuring tartness levels. Complemented by simulation studies, we elucidated the molecular interactions between TA and the borophene/P3MTP composite, revealing how synergistic binding and charge-transfer mechanisms underpin the sensor's enhanced specificity and sensitivity. Developing an electrochemical sensor by combining inorganic and organic materials, employing an aqueous solution, and avoiding harsh chemicals lead to a methodology distinguished by simplicity, affordability, heightened sensitivity, specificity, and sustained stability. This work establishes a foundation for the future development of advanced electrochemical biosensors for applications in food quality assurance, healthcare monitoring, regulatory compliance, and beyond.

2 Materials and methods

2.1 Materials and reagents

3-Methylthiophene (3MTP) (99%), tartaric acid (99%), lithium perchlorate trihydrate (99%), caffeine (99%), and acetone were purchased from Thermo Fisher Scientific. Boron (crystalline 99% trace metals basis), sucrose (≥99.5%), tannic acid, and potassium chloride (KCl) were purchased from Sigma Aldrich. Ethanol was purchased from Changshu Hongsheng Fine Chemical Co. Ltd. Indium tin oxide (ITO) (surface resistivity 8–12 Ω per sq) coated glass was acquired from Sigma Aldrich. Milli-Q water sourced from the laboratory's purification system was utilized for all aqueous solutions and dilutions.

2.2 Apparatus and measurements

The electrochemical tests were carried out using a potentiostat (Admiral Instruments, Squidstat Plus 2332, USA) in a three-electrode configuration. The electrochemical workstation employed in this study is shown in Fig. S1. The working electrode was borophene/P3MTP/ITO@glass, while platinum served as the counter electrode. The reference electrode was Ag/AgCl/Sat. KCl. Polymerization of the monomer solution was conducted using cyclic voltammetry (CV). The Raman spectra were obtained using a DXR2 Raman microscopy spectrometer (Thermo Fisher) with a laser excitation wavelength of 633 nm. The morphological characteristics of borophene were examined using a high-resolution transmission electron microscope (HRTEM) (JEOL JEM 2010) with an accelerating voltage of 200 KV and a point resolution of 0.19 nm.

3 Materials synthesis, construction of the electrode, and computational methods

3.1 Borophene sheet synthesis

Our group has successfully synthesized borophene sheets in our previous studies, as reported in Ranjan *et al.*[48] and Chahal *et al.*[50] We produced borophene from a bulk boron powder using solvent-mediated ultrasonication exfoliation. This synthesis method provides high-quality borophene with excellent structural integrity, paving the way for its use in advanced material applications. The synthesis process started by obtaining bulk boron of high purity. This material serves as the precursor for the synthesis of borophene. The choice of solvent is crucial to facilitate the exfoliation process; it can impact on the quality and characteristics of the resultant borophene. In this study, acetone was used as a solvent to exfoliate the boron sheets. A precise quantity of 0.5 g of bulk boron was weighed and uniformly dispersed in 150 mL of acetone. Ultrasonication was performed for several durations, namely 9 h, 11 h, 13 h, 15 h, and 17 h. After evaluating the results, 15 h was determined to be the optimal period for achieving exfoliation (Fig. S2a). The sample was exposed to ultrasonic waves, generally at

a frequency of 20 kHz or higher, for a prolonged duration, about 15 h. The use of ultrasonic waves induced the formation of cavitation bubbles within the solvent, resulting in the generation of significant shear forces. These forces facilitated the exfoliation process, producing borophene nanosheets from the bulk boron material. Following the ultrasonication procedure, the suspension was centrifuged to achieve the separation of borophene nanosheets from any remaining bulk boron particles. To accomplish this objective, we first collected ultrasonicated bulk boron dispersed in acetone solvent from the upper 1/3rd portion of the bottle. This dispersion was centrifuged for 5 minutes at a speed of 3000 rpm (Fig. S2b). Next, we collected the supernatant and subjected it to another centrifugation for 10 minutes at 7000 rpm (Fig. S2c). Finally, we gathered the supernatant from this final step and preserved it for later use. The supernatant acquired from the experiment was found to contain borophene sheets.

3.2 Electropolymerization of monomer and device fabrication

Firstly, the ITO substrate was subjected to a cleaning procedure, which included immersing it sequentially in acetone, ethanol, and MilliQ water. During each immersion, the substrate was continuously exposed to ultrasonic waves for a period of 10 minutes. Afterward, the substrate underwent a drying process on a hot plate for a duration of 5 minutes. A solution containing 0.01 M of 3MTP monomer was made by dissolving it in MilliQ water and 0.1 M lithium perchlorate ($LiClO_4$). Electropolymerization was employed to transform 3MTP into P3MTP, a conducting polymer. As illustrated in Scheme 1, the electrochemical polymerization of 3MTP was initiated by employing CV. The ITO surface was covered by a conformal covering of P3MTP after five cycles of CV scans across a potential range of 0 to 1.2 V at a scan rate of 50 mV s^{-1}. The overall sensor fabrication process is illustrated in Scheme 1. Borophene sheets were deposited onto the electropolymerized P3MTP film on the ITO surface by drop-casting and then heated at 50 °C on a hot plate to evaporate the solvent, ensuring an even distribution of the borophene sheets over the P3MTP surface.

3.3 Computational methods

The electronic structure calculations were carried out using density functional theory (DFT), employing the projector augmented wave (PAW) method[53,54] as implemented in the Vienna *Ab initio* Simulation Package (VASP).[55–57] The exchange–correlation interactions were treated within the Perdew, Burke, and Ernzerhof (PBE)[58] parameterization under an all-spin polarized framework. Moreover, non-spherical contributions arising from the density gradient within the PAW spheres were explicitly incorporated. Core electrons were substituted with norm-conserving scalar-relativistic pseudopotentials; only valence electrons were explicitly considered in the computations. The valence electron configurations included sulfur (S: $3s^2\ 3p^4$), boron (B: $2s^2\ 2p^1$), oxygen (O: $2s^2\ 2p^4$), and carbon (C: $2s^2\ 2p^2$). To accurately capture van der Waals interactions, we employed Grimme's empirical correction scheme, specifically

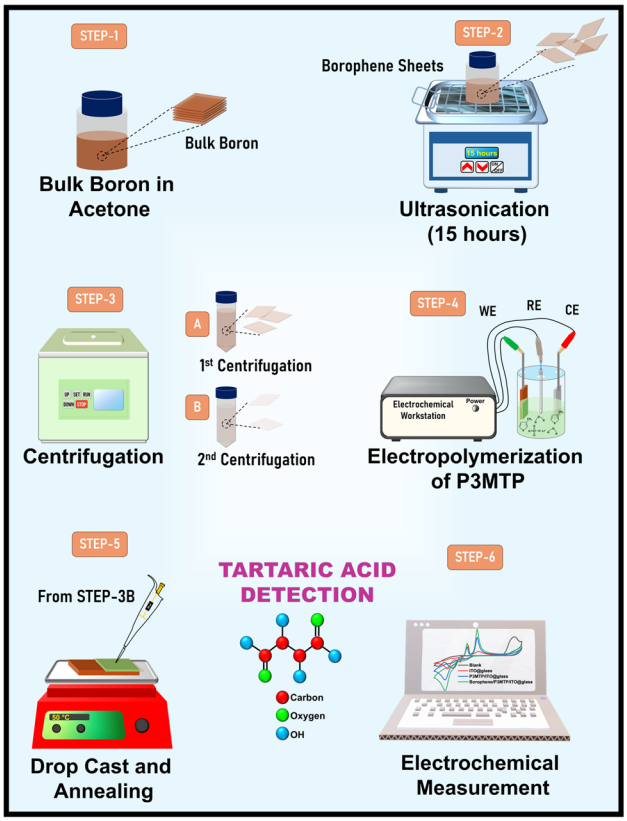

Scheme 1 Schematic representation of the device fabrication process: Step 1 – boron dispersion in acetone; Step 2 – ultrasonication; Step 3 – centrifugation; Step 4 – electropolymerization of P3MTP; Step 5 – drop-casting and annealing; Step 6 – electrochemical measurement.

the DFT + D3 method.[59] The structural models were constructed using a supercell representation of borophene comprising 120 atoms, with a vacuum layer of 15 Å introduced to eliminate spurious interactions between periodic replicas. Energy minimization was performed utilizing a Γ-centered k-point mesh with a K-spacing value of 0.04 $Å^{-1}$ and a plane-wave energy cutoff of 400 eV. The forces acting on the ions were determined *via* the Hellmann–Feynman theorem, and atomic relaxations under spin-polarized conditions proceeded until the residual force on each ion was reduced below 0.01 eV $Å^{-1}$. To elucidate the local charge redistribution in the vicinity of the defect site, Bader charge analysis was conducted.[60] Finally, the binding interactions of TA with both pristine and modified borophene were examined by evaluating their respective binding energies, where the binding energy is calculated by using the following equation, $E_{Bind} = E_{modified\ or\ pristine\ borophene\ with\ TA} - (E_{modified\ or\ pristine\ borophene} + E_{TA})$[61]

4 Results and discussion

4.1 Characterization of materials and modified electrode system

A representative TEM image showing the layered structure of borophene flakes is shown in Fig. 1a, indicating successful

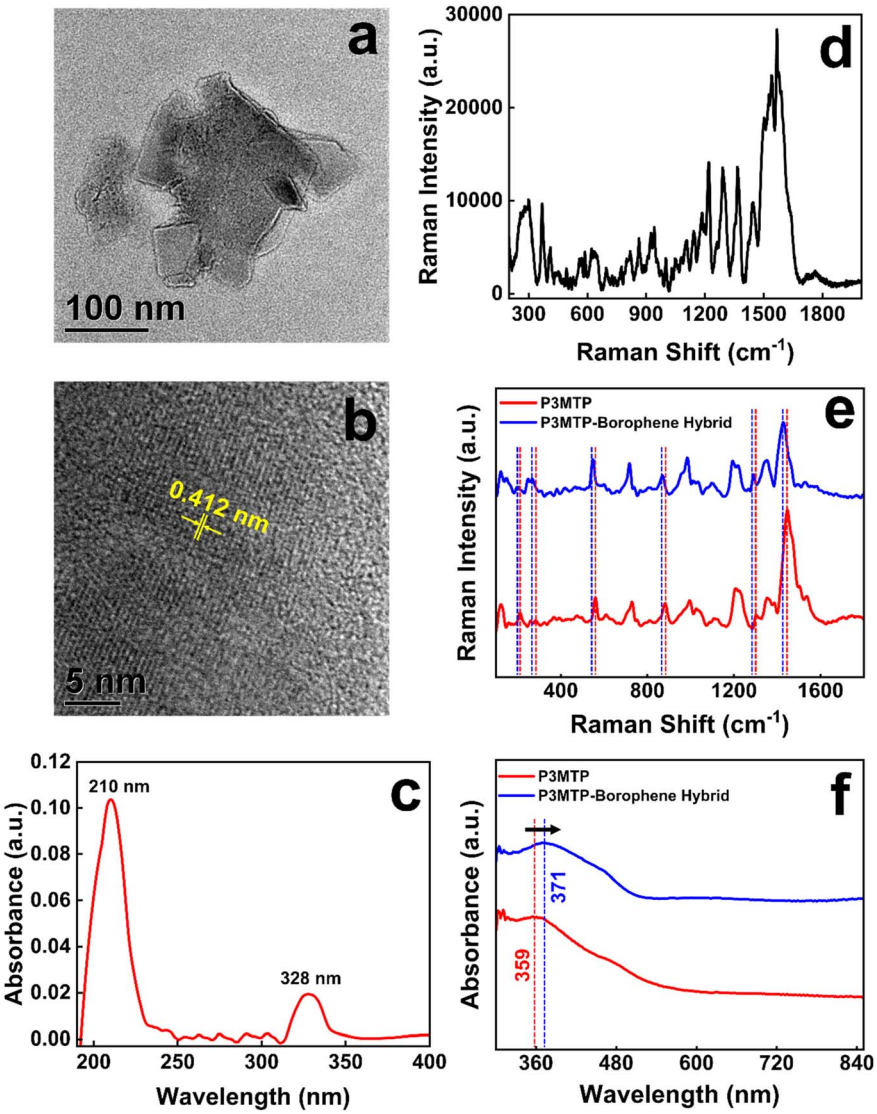

Fig. 1 (a) TEM image, (b) HRTEM image, (c) UV-vis, and (d) Raman spectrum of borophene. (e) Plot illustrating the Raman spectral shifts and (f) UV-vis spectral shifts observed in the hybrid structures.

exfoliation of borophene sheets. A representative HRTEM image (Fig. 1b) displays distinct interference fringes with a d-spacing of 0.412 nm, matching the (104) plane in a β-rhombohedral boron structure.[62] This indicates that the ultrasonic exfoliation in acetone primarily resulted in the physical delamination of borophene sheets without altering the intrinsic crystal structure. Because acetone acts as an inert solvent and does not strongly interact with boron atoms, it facilitates exfoliation while minimizing chemical modification. Thus, the presence of intact lattice fringes supports the crystalline arrangement that is preserved during the process.

Afterward, we analyzed the optical absorption characteristics of the borophene sheet. Fig. 1c displays the absorption spectrum in the UV range. Two absorption peaks were identified at wavelengths of 210 nm and 328 nm. The absorption peak at 210 nm may possibly be attributed to a π–π* transition, whereas the absorption peak observed at 328 nm may be attributable to an n–π* transition in borophene.[63]

Prior studies[64,65] have presented the Raman spectrum of borophene derived through this method, and Fig. 1d illustrates a nearly identical result in the present case. The Raman spectrum shown in Fig. 1d is the far-field analysis of a β_{12} sheet that is nearly one monolayer thick. Several Raman peaks were observed, particularly in the low-frequency range.[64] The Raman spectra analysis of P3MTP and its hybrid counterpart with borophene reveals notable shifts in peak positions across the spectrum. The observed spectral shifts are systematically arranged in ascending order, progressing from the lower-frequency region with a ~9 cm^{-1} shift to the higher-frequency region with a ~18 cm^{-1} shift (Fig. 1e), which reflects significant alterations in the vibrational characteristics and structural properties induced by the incorporation of borophene and can

be attributed to a synergistic effect of charge transfer, interfacial strain, and enhanced electronic interactions.

The UV-visible absorption analysis of P3MTP and its hybrid counterpart with borophene exhibits shifts in peak positions across the spectrum. Specifically, the absorption peak for P3MTP occurs at 359 nm, whereas for the hybrid structure with borophene, it shifts to 371 nm (Fig. 1f). This phenomenon possibly occurs due to the interaction between P3MTP molecules and borophene in the hybrid structure. Borophene's unique electronic properties, such as its surface plasmon resonance or changes in the local electromagnetic field, can alter the absorption characteristics of nearby molecules like P3MTP. These changes manifest as shifts in the UV-visible absorption spectra.

FTIR spectra of P3MTP and its hybrid with borophene show additional peaks after incorporating borophene in the polymer matrix (Fig. S3). The formation of these peaks might be due to the presence of new interlayer vibrational modes that were not present in the pure P3MTP. This is a direct consequence of the new chemical environments created by the incorporation of borophene. In addition, the increased intensity of certain peaks suggests that the new interactions are strong and significantly alter the dipole moment of the molecular bonds. This can be attributed to the high polarizability of borophene and its ability to enhance the interaction strength within the polymer matrix.

DFT-based materials modeling provided a deeper understanding of the interaction between TA and both pristine borophene and a dimer of 3-methylthiophene anchored to borophene. Atomistic simulations were conducted considering the borophene monolayer and the 3-methylthiophene dimer to examine borophene's interaction with P3MTP. Bader charge analysis revealed that boron atoms in borophene undergo charge redistribution upon interaction with TA and the 3-methyl thiophene dimer, with some boron atoms exhibiting charge accumulation while others experience depletion. Specifically, during TA adsorption onto pristine borophene, the average charge gain and loss for boron (B) were calculated to be $-0.85\ e^-$ and $0.94\ e^-$, respectively. When TA interacts with the borophene-anchored 3-methylthiophene dimer, the corresponding values were found to be $-0.87\ e^-$ and $0.92\ e^-$. Although Bader charge analysis suggests only a marginal variation in charge redistribution, the charge density difference map (Fig. 2) distinctly illustrates a pronounced modulation in borophene's charge density due to the interaction. This redistribution of charge density significantly influences the binding energy of TA with both pristine and 3-methylthiophene-modified borophene. The calculated binding energy for TA adsorption on modified borophene is 0.48 eV, compared to 0.44 eV for pristine borophene. Furthermore, various possible configurations of TA and the 3-methylthiophene dimer on borophene were explored, as depicted in Fig. S4.

4.2 Tartaric acid/sourness electrochemical monitoring

The electrochemical CV profile of tartaric acid was assessed using both unmodified and modified electrode systems at various stages of modification. Fig. 3a displays the CV profiles of an unmodified electrode (ITO@glass) and modified electrodes (P3MTP/ITO@glass and borophene/P3MTP/ITO@glass) in a solution of 100 μM tartaric acid with 0.1 M KCl. The blank solution consisted of 0.1 M KCl electrolyte only. KCl serves as an electrolyte in electrochemical systems due to its high ionic conductivity, which reduces resistance and ensures efficient current flow. Being chemically inert, KCl does not interfere with the redox reactions being studied, allowing for accurate measurements of the electroactive species. CV scans were performed using P3MTP/ITO@glass and borophene/P3MTP/ITO@glass electrodes to investigate the electrochemical responses of TA. These scans were conducted over a potential range of −1000 mV to 1500 mV. In the TA-containing electrolyte, the CV analysis of the ITO@glass electrode, used as the control, showed minor redox peaks. Likewise, the borophene/P3MTP/ITO@glass electrode displayed no significant peaks in a blank electrolyte without TA. However, when immersed in the TA-containing electrolyte, the P3MTP/ITO@glass electrode showed distinct behavior. Furthermore, we observed that incorporating P3MTP with borophene (borophene/P3MTP/ITO@glass) led to an additional rise in current density. Modification of the ITO surface with P3MTP and borophene increases the surface area and creates specific sites for TA interaction. TA molecules in the solution adsorb onto the modified electrode surface through interactions such as hydrogen bonding or electrostatic interactions with the polymer's functional groups and the dangling bonds on borophene ridges. Consequently, borophene catalyzed the electrochemical reaction. Our hypothesis can be aligned with the findings of the simulation study conducted by Pei *et al.*[32] In their research, it was demonstrated that the carboxyl oxygen atom and the hydroxyl oxygen atom in the TA molecule engage in interactions with the host material through hydrogen bonding. This insight supports the plausibility of similar interactions occurring in our system. When a potential is applied to the modified electrode, TA undergoes reversible electrochemical oxidation and reduction reactions. It showed two significant oxidation peaks at −0.058 V (Peak 1) and 0.228 V (Peak 2), along with three reduction peaks at −0.183 V (Peak 3), −0.395 V (Peak 4), and −0.687 V (Peak 5), as shown in Fig. 3a. The effect of scan rate (10–150 mV s^{-1}) on the borophene/P3MTP/ITO@glass electrode was analyzed with a fixed 100 μM TA concentration in a 0.1 M KCl solution. As the scan rate increased, the peak currents for all distinguishable peaks also increased, as shown in Fig. 3b. This rise in charging current reduced the diffusion layer, leading to higher peak currents. At higher scan rates (*e.g.*, 50 mV s^{-1} and above), the reduced time for diffusion leads to a thinner diffusion layer, which increases the faradaic (peak) current. Simultaneously, the charging current (non-faradaic) rises proportionally with scan rate. Additionally, faster scan rates shift the system from diffusion-controlled to kinetically controlled regimes, making reaction kinetics more significant.[66,67] The processes occurring at Peak 1, which might be kinetically faster, dominate because the electrochemical reactions outpace the diffusion of the reactants. Thus, Peak 1 current density becomes greater than Peak 2 current density.

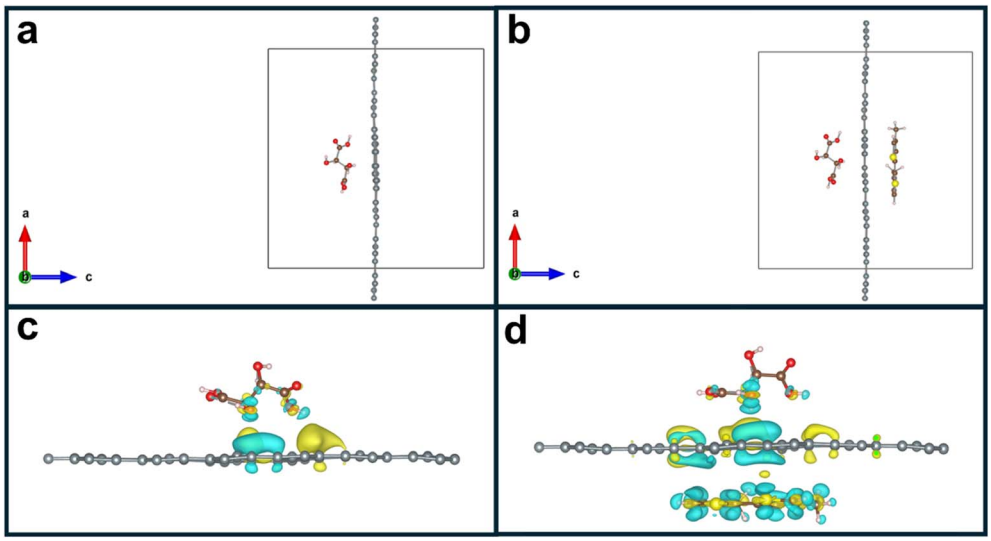

Fig. 2 (a) Optimized structure of TA on borophene, (b) TA and dimer of 3-methylthiophene on the borophene, (c) charge density difference of TA on borophene, and (d) charge density difference of TA with dimer of 3-methylthiophene on the borophene. Grey, red, pink, brown, and yellow balls represent B, O, H, C, and S atoms, respectively. The yellow and blue colors represent the positive and negative isosurfaces at +0.0004 and −0.0004 eV Å^{-3}.

4.3 Concentration-based evaluation

The quantitative assessment of TA was performed under optimal experimental conditions to create a calibration curve for the proposed sensor. This was done using CV as the analytical method. The study examined various concentrations of TA (ranging from 5 to 500 μM) in a 0.1 M KCl supporting electrolyte. The resulting CV showed enhanced signals as the TA concentration increased (Fig. 3c). Using linear regression with the equation $y = 0.6325x + 72.96461$ and $R^2 = 0.99651$, the current density demonstrates a linear relationship, particularly within the range of 5 μM to 300 μM, as illustrated in Fig. 3d. The

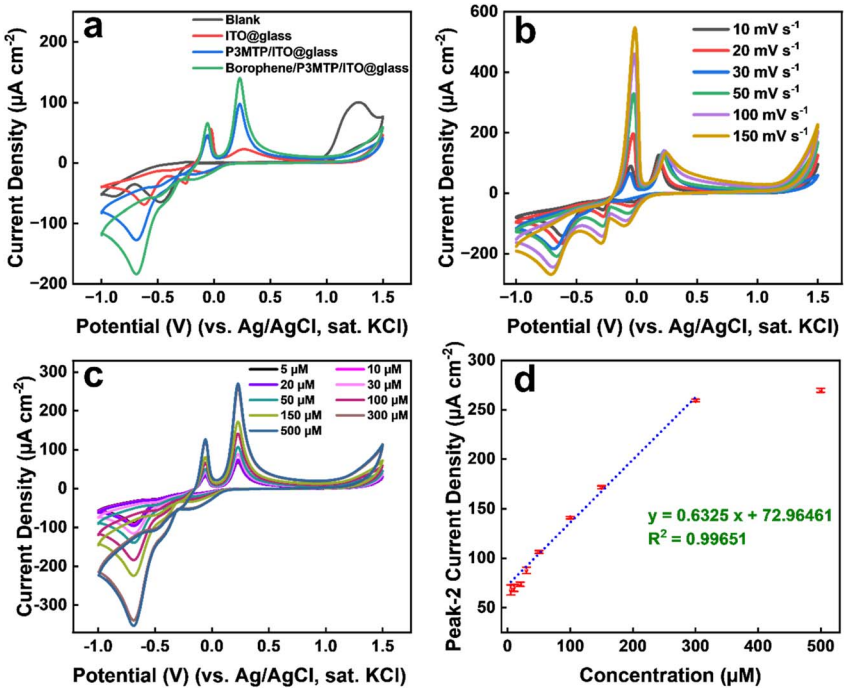

Fig. 3 (a) CV comparison between the modified and unmodified electrodes, conducted in a blank solution and a 0.1 M KCl solution containing 100 μM TA, (b) CV of the modified electrode borophene/P3MTP/ITO@glass using 0.1 M KCl as a supporting electrolyte at various scan rates with a fixed TA concentration of 100 μM. (c) CV profile of the borophene/P3MTP/ITO@glass electrode in 0.1 M KCl supporting electrolyte, scanned at a rate of 30 mV s^{-1} for various concentrations of TA ranging from 5 to 500 μM, and (d) corresponding calibration curve.

LOD was determined through a specific calculation using the formula $3\sigma/S$. In this formula, 'σ' denotes the standard deviation of the peak current density obtained from 10 replicate measurements of the blank at the analyte peak potential, reflecting the variability in the baseline signal, while 'S' represents the slope of the regression plot. The replicate measurements of the blank yielded $\sigma = 0.843$ μA cm^{-2}. The calibration slope, obtained from the linear regression equation, was $S = 0.6325$ μA μM^{-1} cm^{-2}. By applying this formula, the LOD was calculated to be 4 μM. This value signifies the lowest concentration of TA that can be reliably detected using the proposed sensor under the given experimental conditions, demonstrating the sensor's high sensitivity and precision in quantitative analysis. Moreover, all electrochemical measurements in the presence of TA were performed in triplicate ($n = 3$), and the data are reported as mean ± σ. For Peak-2 current density, the values obtained at different TA concentrations (5–500 μM) were 67.94 ± 5.00, 70.01 ± 3.50, 73.72 ± 2.10, 87.84 ± 3.20, 106.45 ± 1.40, 141.11 ± 1.20, 171.77 ± 1.50, 259.48 ± 1.30, and 269.68 ± 2.00 μA cm^{-2}, respectively. Table 1 compares the analytical characteristics of this method for determining TA with prior reports. The sensor reported here exhibited a wide linear range and a low detection limit, making it highly effective for detecting a broad range of TA concentrations. The low detection limit is attributed to the rapid electron transfer rate and increased active surface area provided by the hybrid architecture, which together enhance the sensitivity and signal response of the sensor. Consequently, our study demonstrated the potential of using the borophene/P3MTP/ITO@glass-based electrode for quantitative measurement of TA concentration, which is a surrogate for tartness.

4.4 Selectivity tests

Measurements in the presence of interferents were conducted to assess the specificity of the modified electrode. Caffeine, sucrose, and tannic acid were chosen as additional compounds to assess the interference effect. These species were deliberately chosen because they mimic real-world taste environments, giving rise to astringent, sweet, and bitter sensations, respectively. Their responses were compared with the TA under identical electrochemical conditions (same pH, electrolyte, and applied potential window). The respective interferents were each added to the supporting electrolyte along with TA, each at equal concentrations of 100 μM. Fig. 4a presents the relative current density in the presence of interferents. The relative current densities for Peaks 1, 2, 3, 4, and 5 in the presence of tannic acid were approximately 75–76% of the current densities in the absence of tannic acid, indicating that tannic acid undergoes electrochemical processes under the applied voltages, resulting in a decreased current density response. For sucrose, the relative current densities for Peaks 1, 2, 3, 4, and 5 were about 90–91% of those without sucrose, suggesting a modest reduction in relative current density due to sucrose interference. For caffeine, the relative current densities for Peaks 1, 2, 3, 4, and 5 were approximately 95% of those without caffeine, indicating a minimal decrease in relative current density due to caffeine interference. Collectively, these findings demonstrate that the borophene/P3MTP/ITO@glass electrode exhibits high selectivity for TA, rendering it highly effective for practical applications.

4.5 Stability and reproducibility evaluation

To evaluate the long-term stability of the sensor, we stored it at ambient conditions for up to one month. We conducted periodic assessments of the sensor's functionality at multiple intervals, specifically on Day 1 (immediately following fabrication), Day 7, Day 13, Day 19, Day 25, and Day 31, in each case detecting the response to a 100 μM TA solution. All electrochemical measurements for the stability test in the presence of TA were carried out in triplicate ($n = 3$), and the results are reported as mean ± σ. For Peak-2 current density, the values obtained during the stability evaluation were 141.11 ± 1.20, 130.72 ± 2.10, 124.74 ± 1.80, 121.56 ± 1.20, 116.38 ± 2.10, and 112.79 ± 4.10 μA cm^{-2} from Day 1 to Day 31, respectively. The results consistently demonstrated that the modified electrodes sustained a stable response to TA. This consistent performance underscores the high stability of the modified electrodes, as illustrated in Fig. 4b. To evaluate reproducibility, five independently fabricated borophene/P3MTP/ITO@glass sensors were tested under identical conditions. CV measurements were carried out at a fixed TA concentration of 100 μM, and Peak-2 was considered for evaluation. The RSD% of the peak current response was calculated to be 1.70%, confirming excellent reproducibility of the developed sensor and demonstrating the robustness of the fabrication process. The reproducibility bar plot is depicted in Fig. S5.

Table 1 Modified electrode systems for monitoring TA levels[a]

Modified electrode systems	Method	Linear range (μM)	LOD (μM)	Ref.
$CuGeO_3$NWs@GCE	CV	10–5000	7.7	68
CoPC-CPE	SWV	10–100	7.29	69
La_2O_3/rGO@NiME	CV, DPV	50–1000	151	70
ZrO_2/rGO	DPV	50–1000	22	71
CeO_2/rGO	DPV	50–750	32	72
Borophene/P3MTP/ITO@glass	CV	5–300	4 ($\sigma = 0.843$ μA cm^{-2})	This work

[a] NWs: nanowires; GCE: glassy carbon electrode; CoPC-CPE: cobalt(II)-phthalocyanine-carbon paste electrode; SWV: square wave voltammetry; rGO: reduced graphene oxide; La_2O_3: lanthanum oxide; NiME: nickel mesh electrode; ZrO_2: zirconium dioxide; CeO_2: cerium dioxide.

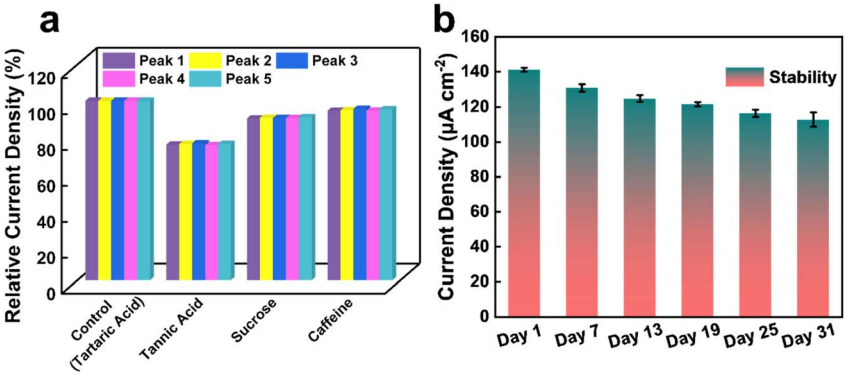

Fig. 4 (a) A plot showing the relative current density of the modified electrode system in an electrolyte with 0.1 M KCl and 100 μM TA (control), along with various interfering species at a scan rate of 30 mV s^{-1}. Each interfering species was present at a concentration of 100 μM. (b) An illustration of the stability of the modified electrode system over various time intervals.

Beyond laboratory-scale demonstration, the fabrication approach employed here is cost-effective, reproducible, and compatible with solution-based processing, which indicates strong potential for scalable production and industrial translation.

5 Conclusions

TA plays a critical role in food quality, human metabolism, and health, necessitating precise detection methods to mitigate risks linked to its abnormal levels. This study introduces a first-of-its-kind electrochemical sensor leveraging a borophene/P3MTP hybrid, which uniquely combines the anisotropic electron transport properties of borophene with the stability of the conducting polymer P3MTP. The sensor's development process, simple, aqueous-based, and free of harsh chemicals, enabled a linear detection range of 5–300 μM and a low LOD of 4 μM, outperforming many conventional TA detection platforms. In addition, the sensor demonstrated high reproducibility, as reflected by a low RSD% of 1.70%. Molecular dynamics simulations revealed unprecedented insights into the synergistic binding and charge-transfer mechanisms between TA and the hybrid, demonstrating how borophene's ridges act as preferential anchoring sites while P3MTP enhances interfacial electron transfer, collectively boosting sensitivity and specificity. The sensor's novelty lies in its dual-material design, which addresses longstanding challenges in TA detection, such as interference from structurally similar organic acids and instability in complex matrices. Unlike existing methods, this platform operates without enzymatic components or costly reagents, ensuring long-term stability. While the findings demonstrate strong potential, the present work is limited to controlled laboratory conditions and a selected set of interference species, without full validation in complex real food matrices. Broader validation in complex food matrices and long-term stability tests remain essential for practical adoption. From a broader perspective, future studies in this field may focus on translating such hybrid platforms into portable point-of-care devices, evaluating performance in diverse real samples, and exploring scalability for industrial production. Extending similar design strategies to other taste-related biomolecules and biohazardous analytes may also provide pathways for developing multifunctional electronic tongues and advanced biosensing platforms with applications in food safety, healthcare, and environmental monitoring.

Author contributions

Shahzad Ahmed: conceptualization, data curation, methodology, investigation, device fabrication, characterizations, visualization, electrochemical data measurements, writing – original draft. Sonal Gupta: visualization, characterization measurements, electrochemical data measurements. Arshiya Ansari: methodology, data curation, figure drawing, investigation, writing – original draft. Tanmay Suresh More: characterization measurements. Andrey N. Kuzmin: characterization measurements. Amitava Banerjee: simulation data measurements, visualization, data curation, writing – review & editing. Devendra Singh Negi: supervision, writing – review & editing. Pranay Ranjan: conceptualization, validation, supervision, writing – review & editing. Mark T Swihart: validation, project administration, supervision, writing – review & editing. Paras N. Prasad: validation, project administration, supervision, writing – review & editing.

Conflicts of interest

The authors declare no competing financial interest.

Data availability

All data supporting the findings of this article are included as a part of supplementary information (SI). Supplementary information: Camera images of electrochemical workstation and borophene exfoliation; FTIR spectra of P3MTP and P3MTP-Borophene hybrid; simulation study of the optimized ground state structure of different orientations of TA on borophene and dimer of 3-methylthiophene on borophene; bar plot illustrating the reproducibility of the fabricated sensor; a table showing

a comprehensive overview of the most recent developments in borophene composites and hybrid-based biosensors. See DOI: https://doi.org/10.1039/d5ra04426j.

Acknowledgements

The Institute for Lasers, Photonics, and Biophotonics acknowledges support from the Office of the Vice President for Research and Economic Development at the University at Buffalo. PR, DSN, and AB would like to acknowledge the funding received from IIT Jodhpur through project number R/I/SEED/PRJ/DSN/AB/20220044. SA would like to acknowledge the financial support provided by the Prime Minister's Research Fellowship (PMRF) for funding this research (PMRF-ID, 2203373). PR, DSN, AB, and SA would like to express gratitude to the Indian Institute of Technology Jodhpur for providing financial and centralized instrumentation facilities.

References

1 B. Ou, H. Rong, B. Cui, J. Zhang and D. Guo, Mechanism of tartaric acid promoting CuO/H_2O_2 Fenton-like degradation of sarafloxacin, *J. Environ. Chem. Eng.*, 2024, **2**, 113225.
2 V. Vijayalakshmi, N. Kanagathara, J. Jan, M. K. Marchewka, A. Mohammad and K. Senthilkumar, Structural, spectroscopic and second harmonic generation evaluation of 1, 2, 4-triazolinium tartrate-tartaric acid as a promising nonlinear optical material, *Opt. Mater.*, 2024, **147**, 114694.
3 J. Su, M. Li, H. Yang, H. Shu, K. Yu, H. Cao, G. Xu, M. Wang, Y. Zhu, Y. Zhu and C. Ma, Enrichment of grape berries and tomato fruit with health-promoting tartaric acid by expression of the Vitis vinifera transketolase VvTK2 gene, *Int. J. Biol. Macromol.*, 2024, **257**, 128734.
4 D. Yang, Z. Li, J. Li, J. Chen, J. Wang, X. Jing and X. Guan, Effect of pre-flowering gibberellic acid applications on tartaric acid content in grape berries, *Sci. Hortic.*, 2024, **325**, 112659.
5 Q. Zhao, G. Du, S. Wang, P. Zhao, X. Cao, C. Cheng, H. Liu, Y. Xue and X. Wang, Investigating the role of tartaric acid in wine astringency, *Food Chem.*, 2023, **403**, 134385.
6 V. Kharb, V. A. Saharan, A. Singh, H. Jadhav, and S. Purohit, *Bitterness Suppression of Oral Pharmaceuticals. The Sense of Taste*, Nova Science Publishers, New York, 2010, 237–276.
7 K. A. Kawale, N. B. Autade, S. H. Narhare and R. L. Mhetrea, A review on fast-dissolving oral film, *Asian. J. Pharm. Clin. Res.*, 2023, **16**(10), 7–17.
8 P. Rai, S. Mehrotra and S. K. Sharma, Challenges in assessing the quality of fruit juices: Intervening role of biosensors, *Food Chem.*, 2022, **386**, 132825.
9 A. Versari, V. F. Laurie, A. Ricci, L. Laghi and G. P. Parpinello, Progress in authentication, typification and traceability of grapes and wines by chemometric approaches, *Food Res. Int.*, 2014, **60**, 2–18.
10 H. Quitmann, R. Fan and P. Czermak, Acidic organic compounds in beverage, food, and feed production, *Biotechnology of Food and Feed Additives*, 2014, 91–141.
11 K. Thakur, D. Singh and R. Rajput, Effects of food additives and preservatives and shelf life of the processed foods, *J. Curr. Res. Food Sci.*, 2022, **3**, 11–22.
12 M. Navarro-Pascual-Ahuir, M. J. Lerma-García, E. F. Simó-Alfonso and J. M. Herrero-Martínez, Quality control of fruit juices by using organic acids determined by capillary zone electrophoresis with poly (vinyl alcohol)-coated bubble cell capillaries, *Food Chem.*, 2015, **188**, 596–603.
13 W. Cui, X. Wang, S. Han, W. Guo, N. Meng, J. Li, B. Sun and X. Zhang, Research progress of tartaric acid stabilization on wine characteristics, *Food Chem.*, 2024, **11**, 101728.
14 M. Li, J. Su, H. Yang, L. Feng, M. Wang, G. Xu, J. Shao and C. Ma, Grape Tartaric Acid: Chemistry, Function, Metabolism, and Regulation, *Horticulturae*, 2023, **9**(11), 1173.
15 W. R. Addington, R. E. Stephens, J. G. Widdicombe, J. W. Anderson and K. Rekab, Effect of tartaric acid–induced cough on pulmonary function in normal and asthmatic humans, *Am. J. Phys. Med. Rehabil.*, 2003, **82**(5), 374–378.
16 A. Jantwal, S. Durgapal, J. Upadhyay, T. Joshi, and A. Kumar, *Tartaric Acid. InAntioxidants Effects in Health*, Elsevier, 2022, 1485–492.
17 V. Garcia-Viñola, C. Ruiz-de-Villa, J. Gombau, M. Poblet, A. Bordons, C. Reguant and N. Rozès, Simultaneous Analysis of Organic Acids, Glycerol and Phenolic Acids in Wines Using Gas Chromatography-Mass Spectrometry, *Foods*, 2024, **13**(2), 186.
18 M. G. Narayanappa, H. Kaipa, A. Chinapolaiah, K. Upreti, A. P. Gowda, D. C. Manjunathagowda, H. H. Venkatachalapathi, S. H. Shekharappa and L. A. Narayanashetty, Exploring gender-based diversity for phenolic and organic acid profiles in the genetic resource of betel vine (Piper betle L.) from India as revealed through high-performance liquid chromatography (HPLC–DAD), *Biotech.*, 2024, **14**(3), 65.
19 P. E. Luner and A. D. Patel, Quantifying crystal form content in physical mixtures of (±)-tartaric acid and (+)-tartaric acid using near infrared reflectance spectroscopy, *AAPS PharmSciTech*, 2005, **6**, E245–E252.
20 H. Cen, Y. Bao, Y. He and D. W. Sun, Visible and near infrared spectroscopy for rapid detection of citric and tartaric acids in orange juice, *J. Food Eng.*, 2007, **82**(2), 253–260.
21 B. Cao and M. Fan. Quantitative analyses of tartaric acid based on terahertz time domain spectroscopy, In. *5th International Symposium on Advanced Optical Manufacturing and Testing Technologies: Optical Test and Measurement Technology and Equipment*, 2010, 7656402–406.
22 S. Mallet, M. Arellano, J. C. Boulet and F. Couderc, Determination of tartaric acid in solid wine residues by capillary electrophoresis and indirect UV detection, *J. Chromatogr. A*, 1999, **853**(1–2), 181–184.
23 H. A. Alhazmi, M. Imran, S. Ahmed, M. Albratty, H. A. Makeen, A. Najmi and M. S. Alam, Electrochemical detection of dopamine using WSe2 microsheets modified platinum electrode, *Phys. Scr.*, 2023, **98**(10), 105006.

24 L. Fritea, F. Bănică, T. O. Costea, L. Moldovan, C. Iovan and S. Cavalu, A gold nanoparticles-Graphene based electrochemical sensor for sensitive determination of nitrazepam, *J. Electroanal. Chem.*, 2018, **830**, 63–71.
25 S. Ahmed, A. Ansari, M. A. Siddiqui, M. Imran, B. Kumari, A. Khan and P. Ranjan, Electrochemical and optical-based systems for SARS-COV-2 and various pathogens assessment, *Adv. Nat. Sci. Nanosci. Nanotechnol.*, 2023, **14**(3), 033001.
26 O. Simoska and K. J. Stevenson, Electrochemical sensors for rapid diagnosis of pathogens in real time, *Analyst*, 2019, **144**(22), 6461–6478.
27 W. D. Adane, B. S. Chandravanshi and M. Tessema, A simple, ultrasensitive and cost-effective electrochemical sensor for the determination of ciprofloxacin in various types of samples, *Sens. Biosens. Res.*, 2023, **39**, 100547.
28 M. A. Munir, F. Rahmawati, J. A. Jamal, S. Ibrahim, M. M. Said and M. S. Ahmad, Inspecting histamine isolated from fish through a highly selective molecularly imprinted electrochemical sensor approach, *ACS Omega*, 2023, **8**(14), 13352–13361.
29 S. Ahmed, A. Ansari, A. S. Haidyrah, A. A. Chaudhary, M. Imran and A. Khan, Hierarchical molecularly imprinted inverse opal-based platforms for highly selective and sensitive determination of histamine, *ACS Appl. Polym. Mater.*, 2022, **4**(4), 2783–2793.
30 S. Ahmed, A. Ansari, S. Bishwanathan, M. A. Siddiqui, S. Tailor, P. K. Gupta, D. S. Negi and P. Ranjan, Electronic Tongue Based on ZnO/ITO@ glass for Electrochemical Monitoring of Spiciness Levels, *Langmuir*, 2024, **40**(8), 4434–4446.
31 A. Khan, S. Ahmed, B. Y. Sun, Y. C. Chen, W. T. Chuang, Y. H. Chan, D. Gupta, P. W. Wu and H. C. Lin, Self-healable and anti-freezing ion conducting hydrogel-based artificial bioelectronic tongue sensing toward astringent and bitter tastes, *Biosens. Bioelectron.*, 2022, **198**, 113811.
32 H. Pei, F. Chen, W. Guo, Q. Jia, R. Guo, N. Liu and Z. Mo, Chiral nitrogen-doped graphene quantum dot electrochemical sensor for recognition of tartaric acid isomers, *J. Electrochem. Soc.*, 2021, **168**(6), 067515.
33 Y. Yang, Y. Liu, L. Song, X. Cui, J. Zhou, G. Jin, A. R. Boccaccini and S. Virtanen, Iron oxide nanoparticle-based nanocomposites in biomedical application, *Trends Biotechnol.*, 2023, **41**(12), 1471–1487.
34 L. Kang, D. He, L. Bie and P. Jiang, Nanoporous cobalt oxide nanowires for non-enzymatic electrochemical glucose detection, *Sens. Actuators, B*, 2015, **220**, 888–894.
35 W. M. Alamier, S. K. Ali, I. Y. Qudsieh, M. Imran, M. Y. Almashnowi, A. Ansari and S. Ahmed, Hydrothermally Synthesized Z-Scheme Nanocomposite of ZIF-9 Modified MXene for Photocatalytic Degradation of 4-Chlorophenol, *Langmuir*, 2024, **40**(11), 6004–6015.
36 A. Abutaleb, S. Ahmed and M. Imran, Synergistic photocatalysis: harnessing WSe2-ZnO nanocomposites for efficient malachite green dye degradation, *Eur. Phys. J. Plus*, 2023, **138**(11), 1046.
37 A. Ansari, S. Ahmed, S. K. Choudhary, M. M. Alam, W. Ali, M. Imran, P. Ranjan and D. S. Negi, Advances in 2D Materials and Hybrid Nanoarchitectures for Gas Sensing Applications, *Adv. Eng. Mater.*, 2025, e202501615.
38 H. Ding, A. M. Hussein, I. Ahmad, R. Latef, J. K. Abbas, A. T. Abd Ali, S. M. Saeed, A. S. Abdulwahid, M. F. Ramadan, H. A. Rasool and A. Elawady, Conducting polymers in industry: A comprehensive review on the characterization, synthesis and application, *Alex. Eng. J.*, 2024, **88**, 253–267.
39 M. Renfige, E. J. Lopez, L. Macor, C. Solis, J. E. Durantini, G. Morales, L. Otero, E. N. Durantini, D. A. Heredia and M. Gervaldo, Electrochemical synthesis of donor-acceptor triazine based polymers with halochromic and electrochromic properties, *Electrochim. Acta*, 2024, **486**, 144120.
40 A. Ansari, S. Ahmed, M. A. Siddiqui, A. Khan, A. Banerjee, D. S. Negi and P. Ranjan, Investigation of complex hybrids in lithium salt under ultraviolet energy source, *J. Mater. Sci.: Mater. Electron.*, 2024, **35**(2), 108.
41 A. Ansari, S. Ahmed, M. A. Siddiqui, A. Khan, S. Tailor, P. Kumar, P. Ranjan and D. S. Negi, PEDOT: PSS, TiO2 Nanoparticles, and Carbon Quantum Dot Composites as Ultraviolet Sensors, *ACS Appl. Nano Mater.*, 2024, **7**(8), 9789–9799.
42 Y. Wang and M. Li, Controlled electropolymerization based on self-dimerizations of monomers, *Curr. Opin. Electrochem.*, 2022, **33**, 100952.
43 J. Heinze, B. A. Frontana-Uribe and S. Ludwigs, Electrochemistry of Conducting Polymers-Persistent Models and New Concepts, *Chem. Rev.*, 2010, **110**(8), 4724–4771.
44 R. A. Vergara and C. A. Binag, Studies on poly (3-methylthiophene)-modified electrode for the electrochemical behavior of dopamine, *KIMIKA*, 2003, **19**(2), 59–67.
45 M. Lu, X. H. Li and H. L. Li, Synthesis and characterization of conducting copolymer nanofibrils of pyrrole and 3-methylthiophene using the template-synthesis method, *Mater. Sci. Eng., A*, 2002, **334**(1–2), 291–297.
46 M. Eguilaz, L. Agüí, P. Yanez-Sedeno and J. M. Pingarrón, A biosensor based on cytochrome c immobilization on a poly-3-methylthiophene/multi-walled carbon nanotubes hybrid-modified electrode. Application to the electrochemical determination of nitrite, *J. Electroanal. Chem.*, 2010, **644**(1), 30–35.
47 V. Sethuraman, P. Muthuraja, M. Sethupathy and P. Manisankar, Development of Biosensor for Catechol Using Electrosynthesized Poly (3-methylthiophene) and Incorporation of LAC Simultaneously, *Electroanalysis*, 2014, **26**(9), 1958–1965.
48 P. Ranjan, T. K. Sahu, R. Bhushan, S. S. Yamijala, D. J. Late, P. Kumar and A. Vinu, Freestanding borophene and its hybrids, *Adv. Mater.*, 2019, **31**(27), 1900353.
49 P. Ranjan, J. M. Lee, P. Kumar and A. Vinu, Borophene: New sensation in flatland, *Adv. Mater.*, 2020, **32**(34), 2000531.

50 S. Chahal, P. Ranjan, M. Motlag, S. S. Yamijala, D. J. Late, E. H. Sadki, G. J. Cheng and P. Kumar, Borophene via micromechanical exfoliation, *Adv. Mater.*, 2021, **33**(34), 2102039.

51 M. A. Ibrahim, A. H. Mahmoud, N. A. Moussa, G. A. Mekhemer, S. R. Sayed, M. N. Ahmed, M. K. Abd El-Rahman, E. Dabbish and T. Shoeib, Adsorption Features of Tetrahalomethanes (CX4; X= F, Cl, and Br) on β 12 Borophene and Pristine Graphene Nanosheets: A Comparative DFT Study, *Molecules*, 2023, **28**(14), 5476.

52 B. N. Šošković, S. Stavrić and Ž. Šljivančanin, Ab-initio and Monte Carlo study of Fe-based two-dimensional magnets at borophene supported by Ag (111) surface, *Phys. Rev. Mater.*, 2021, **5**(7), 074001.

53 G. Kresse and D. Joubert, From ultrasoft pseudopotentials to the projector augmented-wave method, *Phys. Rev. B:Condens. Matter Mater. Phys.*, 1999, **59**(3), 1758.

54 P. E. Blöchl, Projector augmented-wave method, *Phys. Rev. B:Condens. Matter Mater. Phys.*, 1994, **50**(24), 17953.

55 G. Kresse and J. Furthmüller, Efficient iterative schemes for ab initio total-energy calculations using a plane-wave basis set, *Phys. Rev. B:Condens. Matter Mater. Phys.*, 1996, **54**(16), 11169.

56 G. Kresse and J. Furthmüller, Efficiency of ab-initio total energy calculations for metals and semiconductors using a plane-wave basis set, *Comput. Mater. Sci.*, 1996, **6**(1), 15–50.

57 G. Kresse and J. Hafner, Ab initio molecular dynamics for liquid metals, *Phys. Rev. B:Condens. Matter Mater. Phys.*, 1993, **47**(1), 558.

58 G. Kresse and J. Furthmüller, Efficient iterative schemes for ab initio total-energy calculations using a plane-wave basis set, *Phys. Rev. B:Condens. Matter Mater. Phys.*, 1996, **54**(16), 11169.

59 S. Grimme, Semiempirical GGA-type density functional constructed with a long-range dispersion correction, *J. Comput. Chem.*, 2006, **27**(15), 1787–1799.

60 G. Henkelman, A. Arnaldsson and H. Jónsson, A fast and robust algorithm for Bader decomposition of charge density, *Comput. Mater. Sci.*, 2006, **36**(3), 354–360.

61 J. H. Lee, Y. K. Choi, H. J. Kim, R. H. Scheicher and J. H. Cho, Physisorption of DNA nucleobases on h-BN and graphene: vdW-corrected DFT calculations, *J. Phys. Chem. C*, 2013, **117**(26), 13435–13441.

62 F. Zhang, L. She, C. Jia, X. He, Q. Li, J. Sun, Z. Lei and Z. H. Liu, Few-layer and large flake size borophene: preparation with solvothermal-assisted liquid phase exfoliation, *RSC Adv.*, 2020, **10**(46), 27532–27537.

63 D. Ma, J. Zhao, J. Xie, F. Zhang, R. Wang, L. Wu, W. Liang, D. Li, Y. Ge, J. Li and Y. Zhang, Ultrathin boron nanosheets as an emerging two-dimensional photoluminescence material for bioimaging, *Nanoscale Horiz.*, 2020, **5**(4), 705–713.

64 S. Sheng, J. B. Wu, X. Cong, Q. Zhong, W. Li, W. Hu, J. Gou, P. Cheng, P. H. Tan, L. Chen and K. Wu, Raman spectroscopy of two-dimensional borophene sheets, *ACS Nano*, 2019, **13**(4), 4133–4139.

65 M. A. Chowdhury, M. K. Uddin, M. B. Shuvho, M. Rana and N. Hossain, A novel temperature dependent method for borophene synthesis, *Appl. Surf. Sci. Adv.*, 2022, **11**, 100308.

66 N. Elgrishi, K. J. Rountree, B. D. McCarthy, E. S. Rountree, T. T. Eisenhart and J. L. Dempsey, A practical beginner's guide to cyclic voltammetry, *J. Chem. Educ.*, 2018, **95**(2), 197–206.

67 B. J. Venton and Q. Cao, Fundamentals of fast-scan cyclic voltammetry for dopamine detection, *Analyst*, 2020, **145**(4), 1158–1168.

68 Z. Y. Cai, L. Z. Pei, Y. Yang, Y. Q. Pei, C. G. Fan and D. G. Fu, Electrochemical behavior of tartaric acid at CuGeO 3 nanowire modified glassy carbon electrode, *J. Solid State Electrochem.*, 2012, **16**, 2243–2249.

69 A. S. Lourenço, R. F. Nascimento, A. C. Silva, W. F. Ribeiro, M. C. Araujo, S. C. Oliveira and V. B. Nascimento, Voltammetric determination of tartaric acid in wines by electrocatalytic oxidation on a cobalt (II)-phthalocyanine-modified electrode associated with multiway calibration, *Anal. Chim. Acta*, 2018, **1008**, 29–37.

70 M. Mylarappa, S. Chandruvasan, K. S. Harisha and S. C. Sharath, Synthesis, characterization and electrochemical detection of tartaric acid and grape juice using rGO doped La_2O_3 nanoparticles, *Mater. Sci. Eng. B*, 2024, **299**, 116977.

71 M. Mylarappa, S. Chandruvasan, K. S. Harisha and G. Krishnamurthy, Graphene loaded ZrO_2 nanocomposite for antioxidant, dye removal, electrochemical and green sensor studies, *ChemistrySelect*, 2024, **9**(24), e202401218.

72 M. Mylarappa, S. Chandruvasan, K. S. Harisha and G. Krishnamurthy, Development of cerium oxide on rGO: For antioxidant, dye removal, cyclic voltammetry and green sensor studies, *Sustain. Chem. Environ.*, 2024, **7**, 100147.